

# **Final Technical Report: G16AP0004**

## **Models of Earthquake Recurrence on the Imperial Fault Constrained by Surface Deformation Data and Laboratory-Derived Constitutive Laws**

PI: Yuri Fialko

Institute of Geophysics and Planetary Physics, Scripps Institution of Oceanography, University of California San Diego

9500 Gilman Dr., La Jolla, CA 92093-0225

ph. (858) 822-5028

Start date: Jan. 1, 2016

End date: Dec. 31, 2016

## Abstract

We analyzed a suite of geodetic observations across the Imperial fault in southern California that span all parts of the earthquake cycle. Coseismic and postseismic surface slip due to the 1979 M6.6 Imperial Valley earthquake were recorded with trilateration and alignment surveys, and interseismic deformation was measured using a combination of multiple InSAR viewing geometries and continuous and survey-mode GPS. In particular we combined more than 100 survey-mode GPS velocities with InSAR data from Envisat descending tracks 84 and 356 and ascending tracks 77 and 306 (149 total acquisitions), processed using a persistent scatterers method. The result is a dense map of interseismic velocities across the Imperial fault and surrounding areas that allowed us to evaluate the rate of interseismic loading and along-strike variations in surface creep. We compared available geodetic data to models of the earthquake cycle with rate- and state-dependent friction and found that a complete record of the earthquake cycle is required to constrain key fault properties including the rate dependence parameter ( $a - b$ ) as a function of depth, the extent of shallow creep, and the recurrence interval of large events. We found that the data are inconsistent with a high ( $>30$  mm/yr) slip rate on the Imperial fault, and investigated the possibility that an extension of the San Jacinto – Superstition Hills fault system through the town of El Centro may accommodate a significant portion of the slip previously attributed to the Imperial fault. Models including this additional fault are in better agreement with the available observations, suggesting that the long-term slip rate of the Imperial fault is lower than previously suggested, and that there may be a significant unmapped hazard in the western Imperial Valley.

Publications resulting from this project:

Lindsey, E. and Y. Fialko, Geodetic constraints on frictional properties and earthquake hazard in the Imperial Valley, southern California, *J. Geophys. Res.*, 121, 1097-1113, 2016.

## Report

The Imperial fault has hosted several large earthquakes in the past century, the most recent of which was well observed geodetically. The Mw 6.5 October 15, 1979 Imperial Valley earthquake ruptured the northern 30 km of the fault, from just north of the US-Mexico border past the intersection with the Brawley fault, and also triggered some slip on the Brawley fault (Figure 1). Along with detailed mapping of the coseismic surface rupture, postseismic slip observations were collected at several locations along the fault.

A much larger (Mw 7.0) earthquake on the Imperial fault occurred in 1940. The 1940 event ruptured the entire fault and produced up to 6 meters of right-lateral slip near the international border. Paleoseismic evidence at the southern end of the Imperial fault suggests relatively large recurrence intervals and surface offsets (*Thomas and Rockwell, 1996*), while evidence farther north indicates more frequent ruptures with less surface slip.

The Imperial fault is associated with robust shallow creep, first observed there almost 60 years ago, although observations have been mostly limited to the fault section north of the border (e.g. *Crowell et al., 2013*). The creep may be steady or intermittent. In this study, we present observations which indicate that shallow creep does not extend south of the border, and appears to be anti-correlated with coseismic slip from the 1940 event. We use geodetic observations of shallow fault slip that span all parts of the earthquake cycle to constrain the frictional properties of the fault. We also analyze the broader pattern of deformation and identify an active fault strand in the western Imperial Valley that may account for 10 – 15 mm/yr of relative motion between the Pacific and North American plates.

We use Interferometric Synthetic Aperture Radar (InSAR) observations from the European Space Agency’s Environmental Satellite (ENVISAT) spanning the period 2003 - 2010. The satellite collected a total of 149 acquisitions over four tracks covering the Imperial Fault, shown as outlines in Figure 1. There are two descending tracks (356 and 84) and two ascending tracks (77 and 306), providing a dense set of observations from several viewing geometries.

Agricultural activities and the presence of vegetation due to farming in the Imperial Valley severely affects correlation of images at the C-band wavelength of 5.6 cm. We therefore processed this data using a persistent scatterers method (*Hooper et al., 2004*). This method determines a set of stable reflectors based on their amplitude variability, given the observation that those pixels with the least variation in amplitude will also have the most stable phase properties (*Ferretti et al., 2001*). Interferograms for all dates relative to a single master were first calculated using the DORIS software, then the stable reflectors were identified and processed individually. We have identified  $5 \times 10^5$  to  $10^6$  stable pixels for each track, for which velocities were calculated using the Small Baseline Subset (SBAS) method (*Berardino et al., 2002; Schmidt and Bürgmann, 2003*).

The SBAS results contain residual long-wavelength orbital and atmospheric artifacts. We use the sum-remove-filter-restore (SURF) approach to remove them. Horizontal GPS velocities with uncertainties less than 0.5 mm/yr from UNAVCO Plate Boundary Observatory (PBO) and the Southern California Earthquake Center’s Crustal Motion Model 4 were interpolated using a bicubic spline and subtracted from the average LOS velocities for each track. The results were high-pass filtered with a two-dimensional Gaussian filter at a 40 km cutoff wavelength, and then added back to the long-wavelength interpolated GPS map. Because of the filtering step, the result is minimally dependent on the interpolation method and distribution of stations, although we note it may be less accurate south of the U.S. – Mexico border where the distribution of stations is more sparse. In this case, long-wavelength signals may be less accurately represented, however this does not affect our primary goal of an accurate measurement of fault creep.

Using the method described by *Lindsey et al. (2014a)*, we may decompose the ascending and

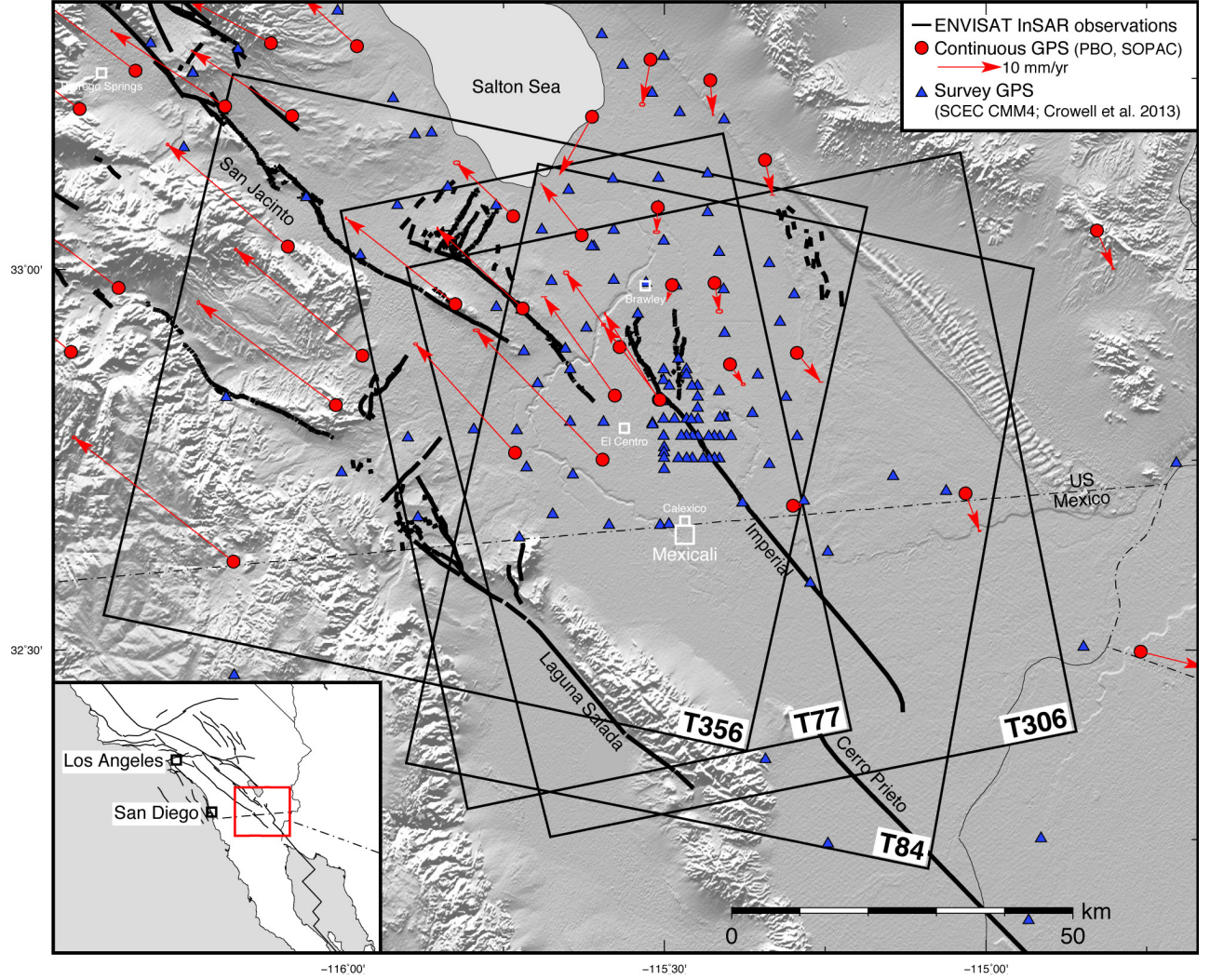


Figure 1: Map showing the study area and nearby faults. Thick black lines with labels denote active faults mapped by the USGS (<http://earthquake.usgs.gov/hazards/qfaults/>). Rectangular outlines show the extent of the ENVISAT InSAR data used in this study. Red dots with vectors show continuous GPS stations with velocity solutions from the Plate Boundary Observatory (PBO, <http://pbo.unavco.org/data/gps>) and the Scripps Orbit and Permanent Array Center (SOPAC, <http://sopac.ucsd.edu>). Blue triangles denote locations of survey-mode GPS monuments. Inset map shows the location in southern California.

descending LOS velocities into vertical and horizontal components, provided the horizontal direction of motion is known and relatively uniform (i.e. predominantly fault-parallel). The GPS velocities shown in Figure 1 suggest this is a reasonable assumption, except for a complex step-over area north of Brawley, which we mask out in our analysis. Because of the properties of radar reflectors on the ground, well-correlated pixels from ascending and descending tracks are not always co-located. Therefore, we first resample the geocoded data with 30 m posting to a coarser 120 m posting using a median filter to maximize the number of co-located pixels in the final results. The results of the velocity decomposition for two independent pairs of ascending and descending tracks are shown in Figure 2, using the average Imperial fault strike of  $N36.5^{\circ}W$  as the direction of horizontal motion.

In addition to the long-wavelength tectonic signal and visible creep along the Superstition Hills and Imperial faults, we note significant non-tectonic motion near areas of active geothermal energy production. In particular, the East Mesa and Heber geothermal areas are associated with significant subsidence visible in all four LOS velocity maps. As seen in Figure 2b and d, subsidence rates exceeding 5 mm/yr are associated with these geothermal areas, with some uplift also visible nearby, possibly related to reinjection. The horizontal velocities (Figures 2a and c) are much less affected by contributions from non-tectonic sources than the LOS velocities, although some anomalies remain. This may be due to a horizontal component of motion related to subsidence, or possibly a temporal aliasing effect due to the different observation times of the ascending and descending tracks.

The Mw 6.6 1979 Imperial Valley earthquake was intensively studied by the U.S. Geological Survey, California Division of Mines and Geology and others, with results reported in USGS Professional Paper 1254 (1982). The results include both detailed field observations of coseismic surface slip and geodetic measurements of afterslip at several locations along the fault.

In addition, we use interseismic velocities from a dense network of GPS monuments in the Imperial Valley, maintained by the Scripps Orbit and Permanent Array Center (SOPAC) and the UNAVCO Plate Boundary Observatory (PBO). Observations are reported in a stable North American reference frame and are available online (<http://pbo.unavco.org/data/gps>). We also combine survey-mode GPS velocities from the Southern California Earthquake Center Crustal Motion Map 4 with a set of campaign data collected and analyzed by *Crowell et al.* (2013). The locations of continuous sites are shown in red, and campaign sites in blue in Figure 1.

Interseismic creep on the Imperial fault has been well documented since it was first observed there in the 1950s. Unlike triangulation and GPS data which can be used to measure horizontal displacements directly, observations of creep using InSAR are complicated by the possibility of differential vertical motion across the fault (Figure 2). By combining the estimated fault-parallel InSAR velocities derived above with campaign GPS velocities where available, we obtain an accurate estimate of the strike-slip creep rate along the northernmost 40 km of the fault.

We select data within a series of 4 km wide, 12 km long profiles across the fault. The profiles are partially overlapping and spaced every 1 km along the length of the fault for which there are InSAR observations from all four tracks, resulting in a total of 43 profiles. The profiles are long enough to be affected by strain accumulation due to long-term fault motion, which adds a trend to the data on either side of the fault. The velocity and strain rate profiles are not necessarily symmetric with respect to the fault trace, as discussed below. To avoid biasing the creep rate estimation, we therefore adopt the method used by *Kaneko et al.* (2013): we fit a linear trend to the data on either side of the fault, and compute the offset between the fitted lines at the location of the fault trace. For each profile, we compute the creep rate for each of the two fault-parallel datasets described above (Figure 2), and combine the results in a least-squares sense.

The results are shown in Figure 3. Uncertainties are shown as the gray area surrounding the best-fit creep rate and are computed as the standard deviation of the residuals for each profile.



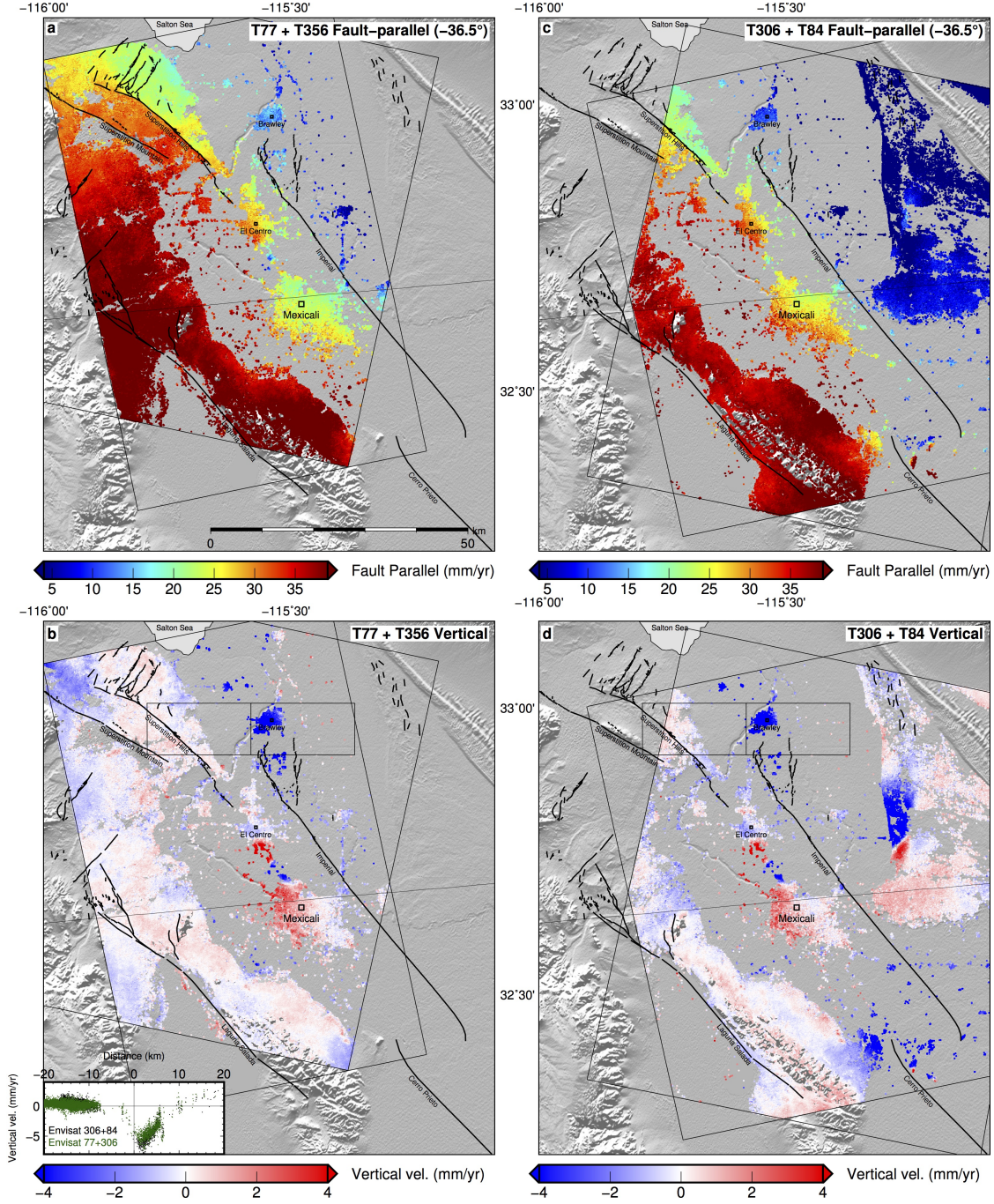


Figure 2: Vertical and fault-parallel components of ENVISAT InSAR observations derived from a combination of two opposing LOS directions using the method of (*Lindsey et al., 2014a*), assuming a constant horizontal direction of motion of N36.5°W. (a) and (c) show the result derived using tracks 77 and 356, while (b) and (d) show the result using tracks 306 and 84.

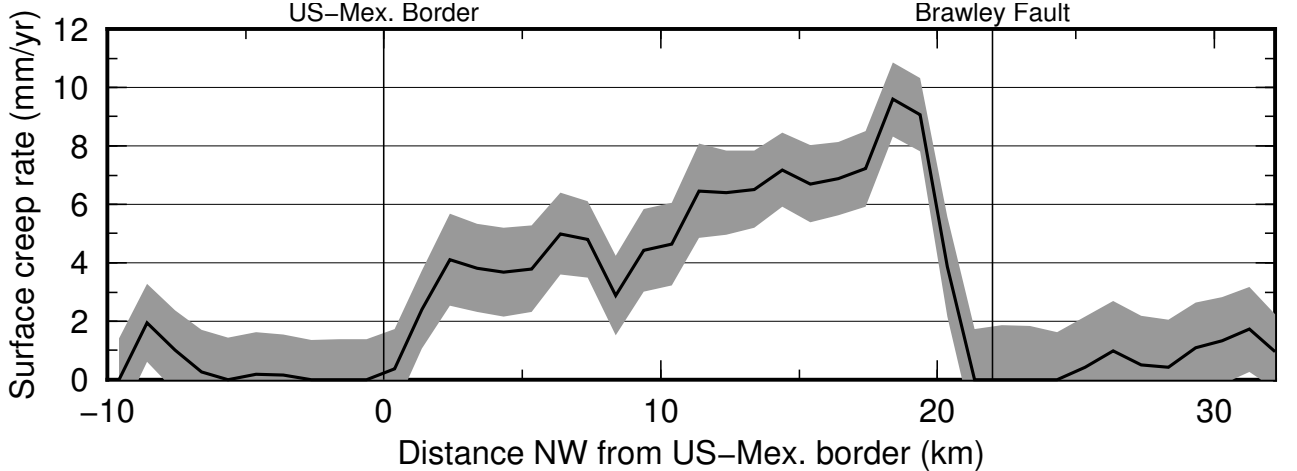


Figure 3: Creep rate along the Imperial fault estimated from fault-parallel InSAR and GPS velocities. Gray shaded area indicates the estimated measurement uncertainty.

Surface creep appears to take place only north of the U.S. – Mexico border, consistent with paleoseismic observations that show no evidence of slip except for the 1940 event just south of the border (*Thomas and Rockwell, 1996*). The rate is typically between 3-8 mm/yr and reaches a maximum of 9-10 mm/yr toward the north, in good agreement with earlier observations (*Crowell et al., 2013*).

Farther to the north, creep appears to stop just before the intersection of the Brawley fault. However, the InSAR data in this area have a lower than average number of persistent scatterers. Also, in 1979 coseismic slip along this part of the fault had a significant dip-slip component, producing subsidence of the Mesquite basin located between the Imperial and Brawley faults. Therefore, the northern terminus of creep is not well established.

Two fault-perpendicular profiles across the InSAR and GPS velocity field are shown in Figure 4. The profiles are 30km wide and include data crossing the fault to the north and south of the international border, respectively. The far-field geodetic data indicate that the relative motion across the Imperial valley is at least 35 – 40 mm/yr. As the Imperial fault is the only mapped active structure at this latitude, this value is typically accepted as a lower bound on its slip rate, and estimated rates of 40 mm/yr or higher are not uncommon (e.g. *Becker et al., 2005*; *Bennett et al., 1996*; *Meade and Hager, 2005*; *Smith and Sandwell, 2003*; *Smith-Konter et al., 2011*).

We fit a simple elastic dislocation model (*Savage and Burford, 1973*) to the data using the method of *Lindsey et al. (2014b)*. We assume a homogeneous elastic half space with dislocations slipping at a constant rate  $s$  below the locking depth  $d_L$ , at a location  $x_L$  that is assumed known. Creep is also permitted at a rate  $c$  between the surface and an assumed depth  $d_C$ , with the creeping fault trace at horizontal location  $x_C$ . The resulting model includes 3 free parameters ( $s, c, d_L$ ), plus a vertical offset value  $v_0$  corresponding to a choice of reference frame. The best-fitting model is found using a Bayesian Monte Carlo method. Before inverting, the InSAR data are first resampled at a constant 0.5 km across-fault spacing by replacing the data with the mean and standard deviation of all pixels within each distance bin. The standard deviation within each bin is used as the uncertainty for that point in the inversion. We combine the GPS and InSAR data by weighting each measurement by its own uncertainty and do not impose an additional dataset-specific weight; however we seek to ensure that some GPS velocities with extremely small uncertainties do not bias the model by imposing a minimum uncertainty of 1mm/yr in the inversion. Finally, we also include

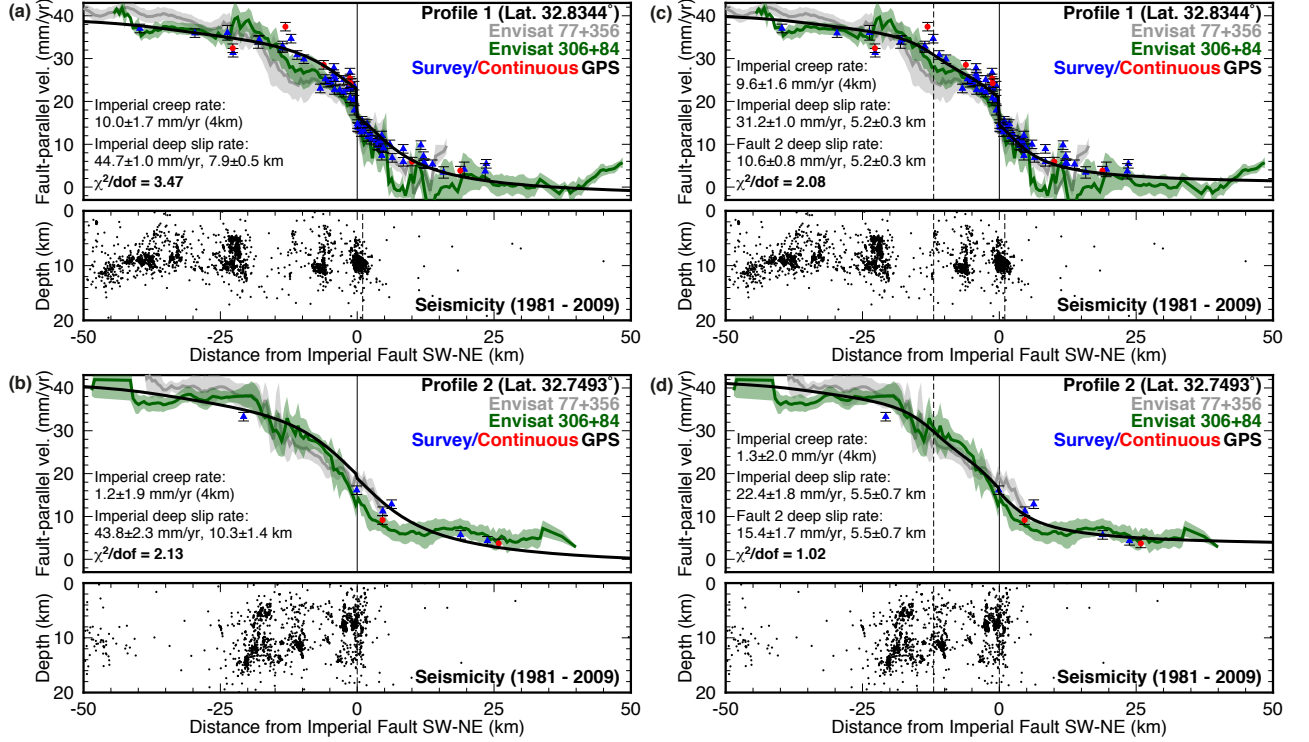


Figure 4: Two profiles across the Imperial fault showing InSAR-derived fault-parallel velocities from tracks 77+306 (gray) and tracks 306+84 (green), and GPS velocities from survey monuments (blue) and continuous stations (red). Panels (a) and (b) include a best-fitting dislocation model with one fault (location shown as dashed line), and (c) and (d) include a best-fitting model with two faults (dashed lines). Model uncertainties are  $2\sigma$  confidence intervals. Microseismicity are from (Hauksson *et al.*, 2012).



the effect of the Elsinore/Laguna Salada fault, located 35 km west of the Imperial fault, by adding a fixed 3 mm/yr dislocation with a 10 km locking depth at that position. This is the same method as adopted by *Lindsey et al.* (2014b) to incorporate the contribution from this less active fault, and is based on geodetic and geologic estimates the slip rate for this fault (*Lindsey and Fialko*, 2013; *Petersen and Wesnowsky*, 1994).

The results are shown in Figure 4, considering the case of a single Imperial fault strand in panels (a) and (b). The fault trace is located at  $x_C = 0$ , and the assumed depth of creep is  $d_C = 4$  km. For the northern profile, seismicity indicates that the fault is dipping slightly to the East, so we allow the deep dislocation to be offset by  $x_L = 1$  km. The best-fitting creep rate is  $10 \pm 1.7$  mm/yr ( $2\sigma$  uncertainty), slightly higher than the measured values in Figure 3. The deep slip rate is nearly 45 mm/yr, close to the full rate of relative motion between the Pacific and North American plates (e.g. *DeMets et al.*, 1994). For the southern profile, the inferred creep rate is indistinguishable from zero, as expected; the deep slip rate is slightly lower than for the northern profile, possibly due to the relatively shorter width of both the InSAR and GPS profiles in this area.

In both cases, there is a systematic misfit between the model and the data. The total geodetic strain accumulated to the west of the fault is significantly higher than that to the east in both profiles; in the southern case as much as 80% of the strain is accumulated to the west of the fault, while the model must place 50% on either side. This strain asymmetry does not coincide with any seismically observed contrast in material properties across the fault, nor does it coincide with significant topography that could result in differential tropospheric delays in the InSAR. One possible explanation is an active sub-parallel fault to the west of the Imperial fault. There are several active lineaments of seismicity to the west of the Imperial fault which extend southward from the mapped traces of the Superstition Hills and Superstition Mountain branches of the San Jacinto fault. Seismicity from the *Hauksson et al.* (2012) catalog (excluding aftershocks of the 2010 Mw 7.2 El Mayor-Cucapah earthquake) are shown as subpanels in Figure 4. The asymmetry in seismicity is clearly evident in both profiles.

Motivated by this observation, we consider a dislocation model with two active faults as shown in Figure 4 panels (c) and (d). We assume the locking depths are the same for both faults, and initially considered the location of the second fault as a free parameter. The best-fitting location was similar in the two profiles ( $11.7 \pm 0.6$  km and  $12.4 \pm 1.8$  km west of the Imperial fault for Profiles 1 and 2, respectively), but the addition of this parameter introduced strong trade-offs with the fault slip rates. We therefore fix the location of the second fault at a distance of 12 km from the Imperial fault, corresponding to a location with both a higher rate of microseismicity and geodetic strain rate in both profiles. The slip rate of the second fault  $s_2$  is considered as an additional free parameter. Because this model has an additional free parameter, a better fit to the data is expected, regardless of whether the model is more representative of the underlying tectonic processes. We can assess whether the improvement in misfit is significant using the Akaike Information Criterion (AIC), defined as  $2k - 2\ln(L)$ , where  $k$  is the number of model parameters and  $\ln(L)$  is the log-likelihood (defined as  $\exp(-\chi^2/N)$ ) of the best-fitting model. In this case, we find that the improvement in fit is significant for both profiles (the AIC value improves from 14.94 to 14.16 for profile 1, and 12.26 to 12.04 for profile 2), suggesting that the addition of a second fault to the model does capture the underlying fault behavior in this region, although the improvement is not large enough to formally rule out the first model.

The inclusion of the additional fault reduces the deep slip rate of the Imperial fault significantly, while the creep rate is relatively unchanged. The inferred slip rate of the proposed fault varies between the two profiles, increasing toward the south from  $10.6 \pm 0.8$  mm/yr to  $15.4 \pm 1.7$  mm/yr. Given the simplicity of this model these rates are not intended to be definitive, but we note that they are in reasonable agreement with inferred slip rates of 10 – 18 mm/yr for the San Jacinto fault

farther north (*Blisniuk et al.*, 2010; *Janecke et al.*, 2010; *Lindsey and Fialko*, 2013; *Lindsey et al.*, 2014b). In our proposed model, this fault transfers slip directly between the San Jacinto fault and the Cerro Prieto fault to the south, eliminating the need for a large transpressional step at the northern end of the Imperial fault.

Kinematic inversions for fault slip rates using geodetic data, such as the model proposed above, have the advantage of a small number of free parameters and are generally successful at explaining the geodetic data in a statistical sense (e.g. *Fay and Humphreys*, 2005; *Lindsey et al.*, 2014b; *Meade and Hager*, 2005; *Smith-Konter et al.*, 2011). However, these models involve strong assumptions about the slip distribution with depth that limit their use in understanding the fault properties that drive such slip. An alternative method is to use numerical models incorporating rate- and state-dependent friction to simulate earthquake cycles on the fault. In these models, the fault stress and rate of slip at all times during an earthquake cycle are estimated in a self-consistent manner, avoiding the dependence on an assumed slip distribution with depth or on an assumed unphysical prestress.

Such models can provide more physical insight into the processes of interseismic slip, shallow fault creep and afterslip, but are computationally intensive and contain many more free parameters.

We consider a vertical fault in a homogeneous elastic half space, governed by rate- and state-dependent friction. The effective shear stress  $\tau(z, t)$  on the fault is given by Equation 1 of *Lapusta et al.* (2000) and includes the radiation damping approximation, which subtracts a term proportional to the slip velocity  $V(z, t)$  so that the integral over the past history of fault slip can be evaluated without encountering singularities. We solve these equations using the fully dynamic adaptive time stepping method described by *Lapusta et al.* (2000). The model domain extends to a depth of 24 km, below which the plate is driven at the constant rate  $V_{pl}$ . The grid size is 12 m, much smaller than the minimum nucleation size (see *Lapusta et al.* (2000)), ensuring a numerically stable solution. In some cases, where stability permitted, we used a grid size of 24 m for computational efficiency. We also ran several test cases with a grid size of 3 and 6 m, and verified that the results were independent of the model discretization.

Models are run for several earthquake cycles until the simulation reaches a cycle-invariant state. For comparison with the observations, we extract a time series of surface displacements for the final cycle. We consider two fault loading rates ( $V_{pl}$ ), 35 mm/yr and 25 mm/yr. The higher rate represents the commonly accepted geodetic slip rate for the Imperial fault, while the lower value corresponds to the case proposed above where some of the strain is accommodated on other active faults to the west. Because the dynamic model formulation is antiplane, we cannot directly include this asymmetric load on the fault. The distant sources of strain would induce a smoothly varying stressing rate across the model depth range, which is not likely to affect the details of post- and interseismic slip, although it could affect the recurrence interval.

Figure 5 shows modeled coseismic and postseismic displacements on the fault at the surface, along with observed displacements from the 1979 Imperial Valley earthquake. When the value of  $(a - b)$  in the top velocity strengthening layer is too small, as in panels (a) and (b), the model produces too much coseismic slip and not enough postseismic slip to fit the data. Conversely, when  $(a - b)$  in the top layer is too large, as in panels (e) and (f), the model does not produce enough coseismic slip, and overpredicts postseismic slip. In panels (c) and (d), the model with the thickest velocity strengthening layer (6 km) shows an unusual acceleration of the postseismic slip after 20 days. This may be related to a stress concentration propagating slowly to the surface; a similar but much smaller delay was observed following the 2004 Parkfield earthquake, where afterslip took up to several hours to reach the surface.

We consider two possible values of the deep driving rate  $V_{pl}$ : 25 mm/yr and 35 mm/yr. The higher value represents the commonly accepted Imperial fault slip rate (e.g. *Smith-Konter et al.*,

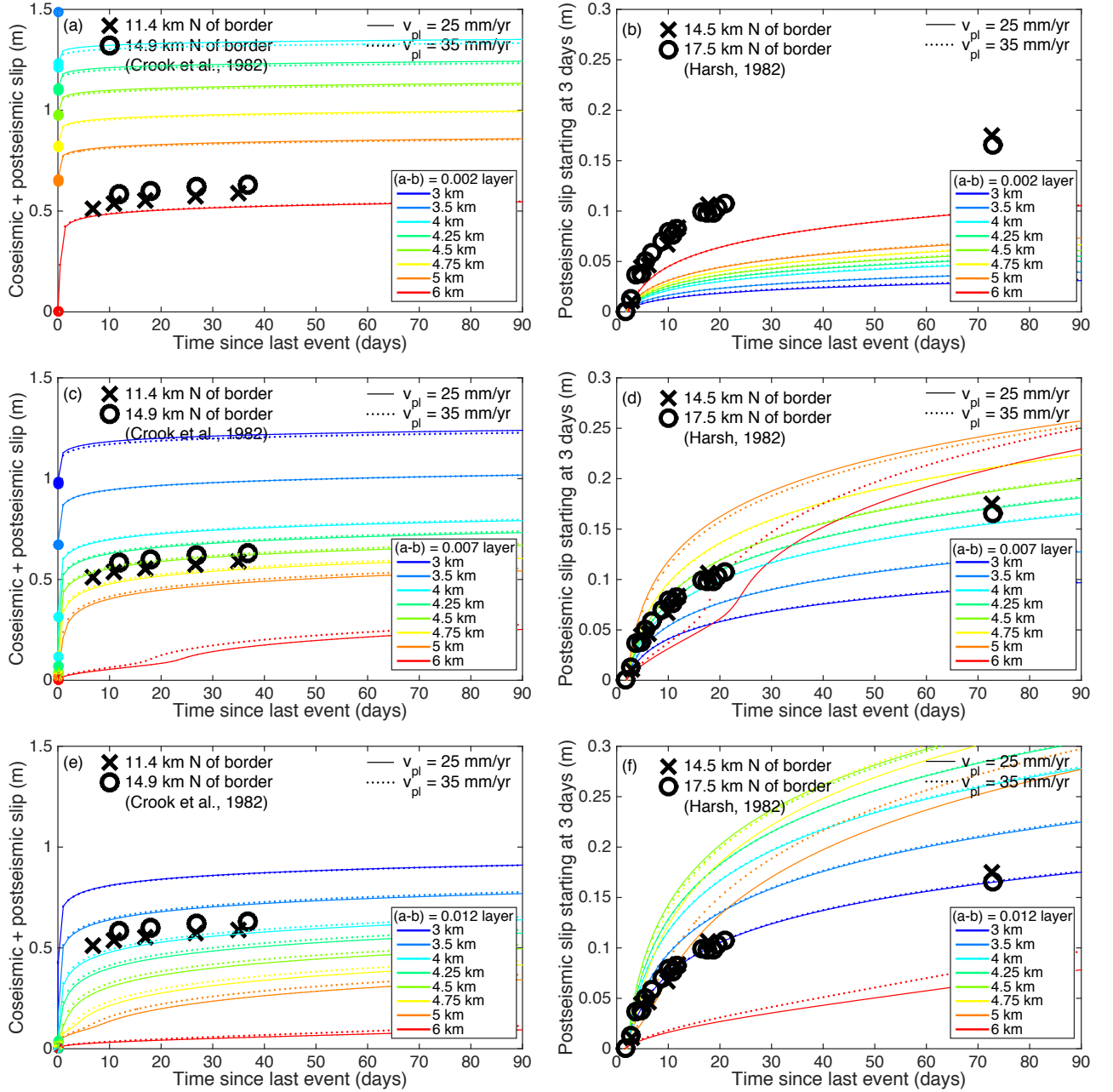


Figure 5: Model predicted surface fault slip (colored lines) compared to observations following the 1979 earthquake (symbols). Panels on the left show the total coseismic + postseismic slip for comparison with trilateration observations, while panels on the right show only postseismic slip, starting at zero three days after the event. Panels (a) and (b) show models where the shallow velocity-strengthening layer has  $(a - b) = 0.002$ ; (c) and (d) have  $(a - b) = 0.007$ ; (e) and (f) have  $(a - b) = 0.012$ .

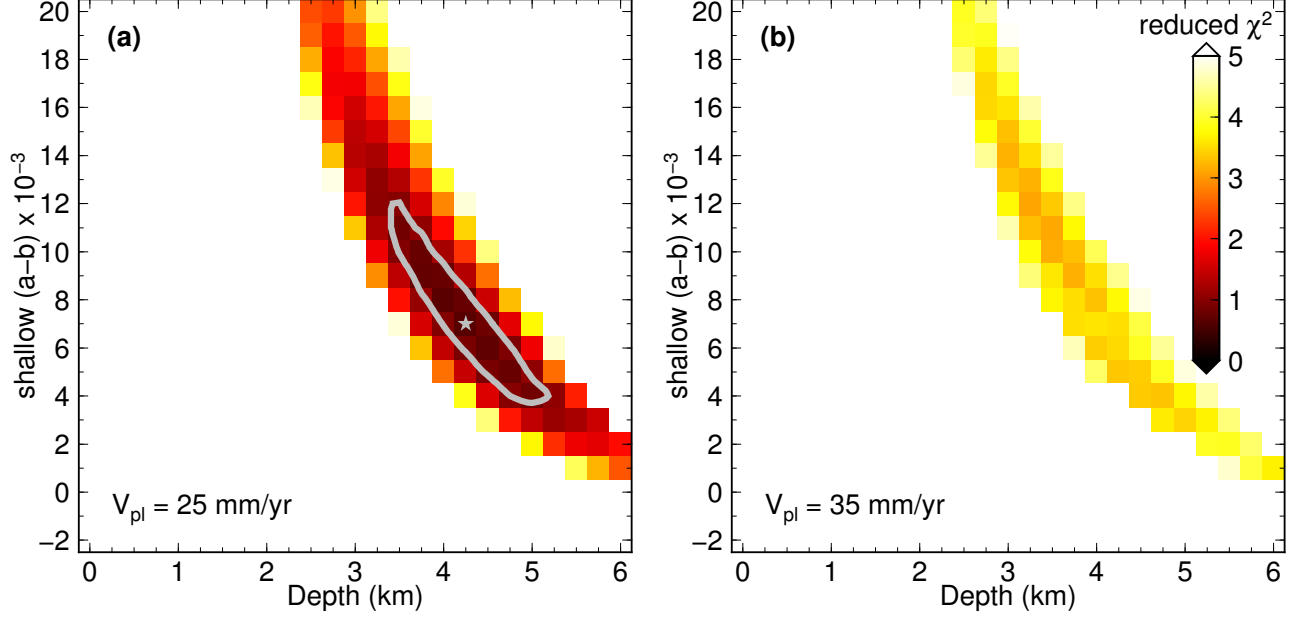


Figure 6: Reduced  $\chi^2$  misfit for the three datasets combined. (a) shows the case of a 25 mm/yr driving rate, and (b) 35 mm/yr driving rate. Starred model corresponds to a velocity-strengthening layer depth of 4.25km with  $(a - b) = 0.007$ .

2011), while the lower value is motivated by our kinematic inversions suggesting slip partitioning between two closely spaced faults. Figure 5 shows that the assumed deep slip rate has almost no effect on the predicted co- and post-seismic displacements. However, the modeled interseismic creep rate is directly proportional to  $V_{pl}$ , so this parameter is a critical factor in determining the overall best-fitting model.

For each model simulation, we compute a  $\chi^2$  misfit to the observations (assuming uncertainties of 10 cm, 2 cm, and 2 mm/yr for the coseismic, postseismic and interseismic datasets respectively). Modeled interseismic creep rates are taken as the minimum surface slip rate observed at any point throughout the earthquake cycle, and are compared against a rate of 7 mm/yr taken from Figure 3 for the part of the fault between 10 - 15 km North of the U.S. - Mexico border, where the coseismic and postseismic observations were collected.

The combined  $\chi^2$  misfit values for all three datasets are shown in Figure 6. We find that for the lower fault slip rate (Figure 6a), a shallow velocity-strengthening layer with values of  $(a - b)$  between  $4 \times 10^{-3}$  and  $1.2 \times 10^{-2}$  and a depth between 3.5 - 5 km can fit all three observations to within the assumed uncertainty. However, for the higher fault slip rate (Figure 6b), there are no sets of parameters that can fit the observations. It is apparent that the misfit is driven by a disagreement between the parameters which can fit the interseismic creep rate and those which fit the co- and postseismic observations. For the lower fault slip rate, the three datasets are in better agreement.

Geodetic observations from InSAR and GPS along the Imperial fault show that creep begins near the U.S. - Mexico border and extends northward, reaching a maximum rate of 9 - 10 mm/yr just south of the intersection with the Brawley fault (Figure 3). These rates are in good agreement with previous observations of the creep at this latitude (Crowell *et al.*, 2013). Creep is not observed to the south of the international border. The data also show an asymmetry in the accumulation of strain with respect to the fault, suggesting that active structures to the west may accommodate a

significant portion of the strain. Models incorporating a second fault to the west provide a better fit to the data (Figure 4).

A lower slip rate on the Imperial fault implied by the two-fault model is also supported by fully dynamic simulations of earthquake cycles on a fault with rate- and state-dependent friction. As shown in Figure 6, a wide range of parameters can reproduce the observed interseismic, coseismic, or postseismic slip along the northern Imperial fault individually, but only a much narrower range of parameters is consistent with all observations.

A lower Imperial fault slip rate of 25 mm/yr is consistent with the proposal that a structure to the west accommodates  $\geq 10$  mm/yr of the relative plate motion, and thereby avoids a transpressional transfer of slip between the northern Imperial and southern San Jacinto faults. The deformation may be localized on one or more major faults with a cryptic surface trace; although there are no mapped faults through this area, the thick sedimentary cover and agricultural disturbance may have prevented their recognition. The deformation could also be accommodated by a larger number of much smaller faults in the basement that are individually difficult to recognize at the surface. During the nearby 2010  $M_w$  7.2 El Mayor – Cucapah earthquake, rupture occurred on several previously unknown faults separated by just a few kilometers from the more well-known Laguna Salada fault, indicating that in this area multiple subparallel faults can coexist close to each other. We also note that when geodetic models of the Southern California fault system are constrained to be consistent with geologic slip rates, they commonly require as much as 30 - 40 % of the relative plate motion to be accommodated off the major faults; this is particularly true in the Imperial valley.

In the case of a 25 mm/yr Imperial fault slip rate, the best-fitting depth of the velocity strengthening layer in our models is  $4.25 \pm 1$  km, in good agreement with the 4 – 4.5 km depth extent of sediment inferred from a seismic refraction survey across this part of the Imperial fault. This is encouraging, given that a rheological change in the fault properties is likely to be correlated with a change in geological structure and composition. However, the micromechanical justification for the sediments to be velocity strengthening is not clear. Moreover, the thick sedimentary cover continues and even deepens south of the U.S. – Mexico border, where creep is not observed.

## Conclusions

We have used geodetic observations to infer in situ frictional properties on the Imperial fault. We find that robust constraints on these properties require observations from all parts of the earthquake cycle. Our results are in good agreement with laboratory-derived values of the slip rate-dependence parameter ( $a - b$ ), for a reasonable range of assumptions. The inferred depth extent of shallow creep is  $\sim 4$  km, in close agreement with the seismically inferred depth of sediments, suggesting a compositional or pore fluid pressure control on the occurrence of stable creep.

Our results also suggest that the Imperial fault is not the only active plate boundary structure at the latitude of the U.S. – Mexico border. Geodetic evidence suggests that significant strain is accommodated by a sub-parallel fault located 10-20 km west of the Imperial fault, which slips at a long-term rate comparable to that of the San Jacinto fault to the north. If so, this fault represents a significant unmapped hazard to the U.S. and Mexican communities of El Centro, Calexico, Heber, and Mexicali.

## References

Ampuero, J., and A.M. Rubin, Earthquake nucleation on rate and state faults - aging and slip laws, *J. Geophys. Res.*, **113**, B01,302, 2008.



- Becker, T. W., J. L. Hardebeck, and G. Anderson, Constraints on fault slip rates of the southern california plate boundary from gps velocity and stress inversions, *Geophys. J. Int.*, *160*, 634–650, 2005.
- Bennett, R. A., W. Rodi, and R. E. Reilinger, Global positioning system constraints on fault slip rates in southern California and northern Baja, Mexico, *J. Geophys. Res.*, *101*, 21,943–21,960, 1996.
- Berardino, P., G. Fornaro, R. Lanari, and E. Sansosti, A new algorithm for surface deformation monitoring based on small baseline differential SAR interferograms, *IEEE Trans. Geosci. Rem. Sens.*, *40*, 2375–2383, 2002.
- Blisniuk, K., T. Rockwell, L. A. Owen, M. Oskin, C. Lippincott, M. W. Caffee, and J. Dortch, Late Quaternary slip rate gradient defined using high-resolution topography and  $^{10}\text{Be}$  dating of offset landforms on the southern San Jacinto Fault zone, California, *J. Geophys. Res.*, *115*, B08,401, doi:10.1029/2009JB006,346, 2010.
- Crowell, B. W., Y. Bock, D. T. Sandwell, and Y. Fialko, Geodetic investigation into the deformation of the Salton Trough, *J. Geophys. Res.*, *118*, 5030–5039, doi:10.1002/jgrb.50347, 2013.
- DeMets, C., R. G. Gordon, D. F. Argus, and S. Stein, Effect of recent revisions to the geomagnetic reversal time scale on estimates of current plate motions, *Geophys. Res. Lett.*, *21*, 2191–2194, 1994.
- Dieterich, J. H., Earthquake nucleation on faults with rate- and state-dependent strength, *Tectonophysics*, *211*, 115–134, 1992.
- Fay, N., and G. Humphreys, Fault slip rates, effects of elastic heterogeneity on geodetic data, and the strength of the lower crust in the Salton Trough region, southern California, *J. Geophys. Res.*, *110*, B09,401, doi:10.1029/2004JB003,548, 2005.
- Ferretti, A., C. Prati, and F. Rocca, Permanent scatterers in sar interferometry, *IEEE Trans. Geosci. Rem. Sens.*, *39*, 8–20, 2001.
- Hauksson, E., W. Yang, and P. M. Shearer, Waveform relocated earthquake catalog for southern california (1981 to 2011), *Bull. Seism. Soc. Am.*, *102*(5), 2239–2244, doi:10.1785/0120120010, 2012.
- Hooper, A., H. Zebker, P. Segall, and B. Kampes, A New Method for Measuring Deformation on Volcanoes and Other Natural Terrains Using InSAR Persistent Scatterers, *Geophys. Res. Lett.*, *31*, doi:10.1029/2002GL016,156, 2004.
- Janecke, S. U., et al., High geologic slip rates since early Pleistocene initiation of the San Jacinto and San Felipe Fault zones in the San Andreas Fault system, Southern California, USA, *GSA Special Papers*, *475*, 1–48, 2010.
- Kaneko, Y., Y. Fialko, D. Sandwell, X. Tong, and M. Furuya, Interseismic deformation and creep along the central section of the North Anatolian Fault (Turkey): InSAR observations and implications for rate-and-state friction properties, *J. Geophys. Res.*, *118*(1), 316–331, 2013.
- Lapusta, N., J. Rice, Y. Ben-Zion, and G. Zheng, Elastodynamic analysis for slow tectonic loading with spontaneous rupture episodes on faults with rate- and state-dependent friction, *J. Geophys. Res.*, *105*(B10), 23,765–23,789, doi:10.1029/2000JB900250, 2000.
- Lindsey, E., and Y. Fialko, Geodetic slip rates in the Southern San Andreas Fault System: Effects of elastic heterogeneity and fault geometry, *J. Geophys. Res.*, *118*, 689–697, 2013.
- Lindsey, E. O., Y. Fialko, Y. Bock, D. T. Sandwell, and R. Bilham, Localized and distributed creep along the southern San Andreas Fault, *J. Geophys. Res.*, *119*(10), 7909–7922, 2014a.
- Lindsey, E. O., V. J. Sahakian, Y. Fialko, Y. Bock, S. Barbot, and T. K. Rockwell, Interseismic strain localization in the San Jacinto fault zone, *Pure and Applied Geophysics*, *171*(11), 2937–2954, 2014b.
- Meade, B. J., and B. H. Hager, Block models of crustal motion in southern California constrained by GPS measurements, *J. Geophys. Res.*, *110*, Art. No. B03,403, doi:10.1029/2004JB003,209, 2005.
- Petersen, M. D., and S. G. Wesnousky, Fault slip rates and earthquake histories for active faults in Southern California, *Bull. Seism. Soc. Am.*, *84*, 1608–1649, 1994.
- Savage, J., and R. Burford, Geodetic determination of relative plate motion in central California, *J. Geophys. Res.*, *78*, 832–845, 1973.
- Schmidt, D., and R. Bürgmann, Time-dependent land uplift and subsidence in the Santa Clara valley, California, from a large interferometric synthetic aperture radar data set, *J. Geophys. Res.*, *108*, 2416, doi:10.1029/2002JB002,267, 2003.
- Smith, B., and D. Sandwell, Coulomb stress accumulation along the San Andreas Fault system, *J. Geophys. Res.*, *108*, 10.1029/2002JB002,296, 2003.

- Smith-Konter, B. R., D. T. Sandwell, and P. Shearer, Locking depths estimated from geodesy and seismology along the san andreas fault system: Implications for seismic moment release, *J. Geophys. Res.*, *116*(B6), 2011.
- Thomas, A. P., and T. K. Rockwell, A 300- to 550-year history of slip on the Imperial fault near the U.S.-Mexico border: Missing slip at the Imperial fault bottleneck, *J. Geophys. Res.*, *101*, 5987–5997, 1996.